

[Supporting information](#)

**Tunable Syngas Production from Photocatalytic CO<sub>2</sub>  
Reduction with Mitigated Charge Recombination Driven by  
Spatially Separated Cocatalysts**

Ang Li<sup>1</sup>, Tuo Wang<sup>1</sup>, Xiaoxia Chang, Zhi-Jian Zhao, Chengcheng Li, Zhiqi Huang,  
Piaoping Yang, Guangye Zhou, and Jinlong Gong\*

*Key Laboratory for Green Chemical Technology of Ministry of Education, School of  
Chemical Engineering and Technology, Tianjin University; Collaborative Innovation  
Center of Chemical Science and Engineering (Tianjin), Tianjin 300072, China*

\*Email: jlgong@tju.edu.cn

<sup>1</sup> *These authors contributed equally to this work*

## Experimental Procedures

### Materials

Platinum acetylacetonate ( $\text{Pt}(\text{acac})_2$ ) was purchased from J&K. Copper acetylacetonate ( $\text{Cu}(\text{acac})_2$ ) was purchased from Heowns.  $\text{KMnO}_4$  was purchased from Jiangtian. Aqueous ammonia was purchased from Kemiou. Tetraethyl orthosilicate (TEOS, 98%) was purchased from Tianjin Chemical Reagent No. 1 Plant. Titanium tert-butoxide (TBOT,  $\geq 98.0\%$ ) ( $\geq 99.0\%$ ) was purchased from Sinopharm. Methanol and ethanol were purchased from Guangfu. Poly (4-vinylpyridine) (PVP) and hydroxypropyl cellulose (HPC) were purchased from TCI.  $\text{Na}_2\text{SO}_3$  was purchased from Yuanli.  $\text{KHCO}_3$  was purchased from Macklin. Deionized water ( $18.25 \text{ M}\Omega \cdot \text{cm}$ ) supplied by an UP Water Purification System was used in the whole experimental processes. All chemicals were obtained from commercial suppliers and used without further purification.

### Characterization

Transmission electron microscope (TEM) was performed on a JEOL JEM 2100F electron microscope. Photoluminescence (PL) spectrum was performed on a Hitachi F-4600 fluorescence spectrophotometer. BET surface area and pore structure of catalysts were measured using a Micromeritics Tristar 3000 analyzer by nitrogen adsorption at 77 K. The specific surface areas were calculated from the isotherms using the BET method. The pore distribution and the cumulative volumes of pores were obtained by the BJH method from the adsorption branch of the adsorption isotherms. Inductively Coupled Plasma Optical Emission Spectrometer (ICP-OES) was performed on a Vista MPX ICP. *In situ* infrared spectrometer patterns were performed on a thermo scientific iS50 FT-IR. XPS was performed under ultrahigh vacuum ( $<10^{-6} \text{ Pa}$ ) on a Kratos XSAM 800 spectrometer with Mg Ka X-ray source ( $E = 1253.6 \text{ eV}$ ).

### Methods

**1. Synthesis of  $\text{MnO}_x @ \text{TiO}_2$  mesoporous hollow spheres (MT-MSs).** TEOS (0.8 mL) was mixed with deionized water (5 mL),  $\text{KMnO}_4$  (0.01 g), ethanol (20 mL) and the aqueous ammonia (0.4 mL). Ethanol acts as dispersant and reductant to produce  $\text{MnO}_x$  from  $\text{KMnO}_4$ . In alkaline environment, the oxidizability of  $\text{KMnO}_4$  is weak enough to

produce  $\text{MnO}_x$  slowly, forming small and uniform  $\text{MnO}_x$  particles. After stirring for 6 h, the precipitated silica spheres loaded with  $\text{MnO}_x$  ( $\text{SiO}_2\text{-MnO}_x$ ) were separated by centrifugation and washed twice with ethanol, then re-dispersed in 5 mL ethanol under sonication. Subsequently, the suspension was mixed with ethanol (20 mL), deionized water (0.1 mL) and HPC (0.1 g). After 30 min stirring, 5 mL of 2.84 M TBOT ethanol solution was injected into the mixture at a rate of 0.75 mL/min. After injection, the temperature was increased to 85 °C with stirring under refluxing conditions for 100 min to give  $\text{SiO}_2\text{-MnO}_x\text{@TiO}_2$  core-shell structures. The precipitate was isolated using centrifugation, washed twice with ethanol and water, and then dispersed in 20 mL PVP (0.14 g) solution. After 12 h, the precipitate was separated, re-dispersed in ethanol (20 mL), and then mixed with water (5 mL), TEOS (0.4 mL) and aqueous ammonia (0.4 mL) to form the  $\text{SiO}_2$  outermost protective layer. TEOS was added at twice with the interval of 30 min. After stirring for 6 h, the resulting  $\text{SiO}_2\text{-MnO}_x\text{@TiO}_2\text{@SiO}_2$  composites were centrifuged, washed three times with ethanol and dried under 80 °C for 12 h. Subsequently, the above powders were calcined in air for another 2 h at 500 °C. Then the calcined samples were dispersed in 20 mL water under sonication and heated to 70 °C. 1 mL of 1.67 M aqueous NaOH solution was added to the above suspension.  $\text{SiO}_2$  easily reacts with NaOH following the equation:  $\text{SiO}_2 + 2\text{NaOH} \rightarrow \text{Na}_2\text{SiO}_3 + \text{H}_2\text{O}$ .  $\text{Na}_2\text{SiO}_3$  is highly soluble in water thus can be selectively removed to create a void space.<sup>1</sup> After etching for 8 h, the precipitate was isolated using centrifugation, washed twice with water and dried under 80 °C for 12 h, and then MT-MSs were formed.

**2. Synthesis of  $\text{MnO}_x\text{@TiO}_2\text{@CuPt}$  alloy mesoporous hollow spheres with different ratios of Cu:Pt ( $\text{MTC}_x\text{P-MSs}$ ).** MT-MSs powders (0.05 g),  $\text{Pt}(\text{acac})_2$  and  $\text{Cu}(\text{acac})_2$  were mixed in 40 mL methanol, and the suspension was then irradiated by a 300 W Xe lamp ( $\lambda < 420$  nm) under continuous stirring under the protection of  $\text{N}_2$ . After 5 h photo-deposition, the precipitate was isolated using centrifugation, washed with deionized water many times until the last cleaning liquid is close to  $18.25 \text{ M}\Omega\cdot\text{cm}$ , and finally dried at 60 °C for overnight to produce  $\text{MTC}_x\text{P-MSs}$  structures. Then the powder was calcined again in air at 200 °C for 2 h to enhance the interaction of components and ensure the decomposition of carbon containing pollutants. By changing the feed ratio of  $\text{Pt}(\text{acac})_2$  and  $\text{Cu}(\text{acac})_2$ , the ratio of Cu and Pt can be adjusted. This ratio in the finished product was determined to be 0.31:1, 1.13:1, 3.17:1 and 8.72:1

by ICP-OES, denoted as  $\text{MTC}_{0.31}\text{P-MSs}$ ,  $\text{MTC}_{1.13}\text{P-MSs}$ ,  $\text{MTC}_{3.17}\text{P-MSs}$  and  $\text{MTC}_{8.72}\text{P-MSs}$ , respectively.

**3. Synthesis of  $\text{TiO}_2$  mesoporous hollow spheres (T-MSs) and  $\text{TiO}_2/\text{MnO}_x/\text{Cu}_{3.21}\text{Pt}$  alloy mesoporous hollow spheres (T/M/ $\text{C}_{3.21}\text{P-MSs}$ ) and  $\text{Cu}_{3.12}\text{Pt}@\text{TiO}_2@\text{MnO}_x$  ( $\text{C}_{3.12}\text{PTM-MSs}$ ).** By repeating steps of the synthesis of MT-MSs without adding  $\text{KMnO}_4$ , the T-MSs were synthesized. To synthesize the T/M/ $\text{C}_{3.21}\text{P-MSs}$ , a T-MSs core-shell structure was synthesized at first, then Pt and  $\text{MnO}_x$  were loaded by impregnation method. The Cu/Pt ratio was determined to be 3.21:1 by ICP-OES, which is similar to the Cu content of  $\text{MTC}_{3.17}\text{P-MSs}$ .  $\text{C}_{3.12}\text{PTM-MSs}$  was synthesized by the traditional method for cocatalysts separated structures.

**4. Photocatalytic  $\text{CO}_2$  reduction.** The home-made photocatalytic reactor is consisted of a sealed chamber, an embedded window made by quartz glass and a liquid sampling port sealed by silicone pad. The reactor was connected to a gas circulation system with a ten-port valve (VICI) for on-line sampling to a gas chromatograph (GC, Ruimin GC 2060, Shanghai). The gas circulation system was primarily made of stainless steel tubing and a customized mechanical circulation pump for gas circulation. The mechanical pump was connected into the system to exhaust the carrier gas of the gas chromatograph when switch back the ten-port valve. A pressure gauge was also connected to the system to monitor the pressure. The total volume of the gas in the circulation system after filling the reactor with solvent was 80 mL. Measurable tube (1 mL) of GC was also involve in this closed system. The ratio of total volume for gas in the circulation system to the volume of measurable tube was defined as the volume factor.

Before the start of reaction, 0.08 g catalysts were mixed with 40 mL  $\text{KHCO}_3$  (0.1 M, to enhance the solubility of  $\text{CO}_2$ ) and  $\text{Na}_2\text{SO}_3$  (0.1 M, acting as holes sacrifice agent) aqueous solution in the reactor, then the system was evacuated to remove air. Subsequently, the suspension in reactor was purged with  $\text{CO}_2$  ( $\geq 99.995\%$ ) for 1 h to achieve  $\text{CO}_2$  saturation and the initial  $\text{CO}_2$  pressure was kept at atmospheric pressure. There was no more  $\text{CO}_2$  purged into the closed system during the reaction. The gases in the closed circulation system were continuously circulated through the suspension for the entire reaction period. The reactions were carried out under  $100 \text{ mW/cm}^2$  AM 1.5G illumination. After 1 h of irradiation, gas in measurable tube was injected into the

GC by switch back the ten-port valve for analysis. The amount of generation for every component during 1 h is the generation rate, which means product generation during unit time. To avoid the error caused by the volume change and gas leakage during the switch of valve, after the irradiation, the catalysts were separated by centrifugation and used for another 1 h following similar operation process. After three times, the average value and standard deviation of the results are exhibited as the production rate and error bar.

The analysis of the gaseous reaction mixtures containing CO, CH<sub>4</sub>, H<sub>2</sub>, was carried out using a gas chromatograph, which was equipped with a TCD, an FID and a methanizer which contained Ni catalyst. Argon ( $\geq 99.999\%$ ) was used as the carrier gas. The back channel of GC was equipped with two packed columns, TDX-01 and Molsieve 5 Å, and two gas switching valves. During the analysis, 1.0 mL of gas sample in the sample loop of ten-port valve was introduced to the TDX-01 column where CO<sub>2</sub> was separated from the other gases due to its longer retention time. The rest of the gases after the TDX-01 column was further separated by the Molsieve 5 Å column. The gas product of H<sub>2</sub> was detected by TCD and CH<sub>4</sub>, CO were further detected by FID with higher sensitivities. The role of methanizer was to convert CO to CH<sub>4</sub> for FID analysis. External standard method was used to calculate of amount of every component from the peak area of GC. Specifically, gas of known amount was injected into GC and the peak areas of every amount was recorded, which can be used to make a standard table to exhibit the relationship between area peaks and product amounts by data fitting. Based on the relationship, we can calculate the amount of every component from the peak area of GC.

The stability test was operated by the investigation of the activity of every catalyst during 4 circles. After every circle, the catalysts were separated by centrifugation and used for next circle. Considering every circle last 3 h, actually the test exhibited the stability of catalysts during 12 h.

**5. The calculation of overall conversion yield ( $\eta$ ).** The overall conversion yield was calculated as follows<sup>2</sup>:  $\eta (\%) = [R(\text{CO}) \times \Delta G^\circ] / [P \times S] \times 100\%$ , where R(CO),  $\Delta G^\circ$ , P, and S denote the rate of carbon monoxide evolution ( $\text{mol s}^{-1}$ ) in the photocatalysis, the change in the Gibbs free energy that accompanies the CO<sub>2</sub> photoreduction to CO ( $64.1 \times 10^3 \text{ J mol}^{-1}$ ), the energy intensity of the solar light irradiation ( $0.1 \text{ W cm}^{-2}$ ), and

the irradiation area (13.9 cm<sup>2</sup>), respectively. In some previous papers,  $\eta$  was not supplied directly. For comparison purposes, we calculate  $\eta$  according to this equation. Additionally, for papers lacking of the information of irradiation area, we adopted the general value of 13.9 cm<sup>2</sup>.<sup>3,4</sup>

**6. In-suit infrared.** About 20 mg catalysts loaded on the sample cell of diffuse reflectance attachment and make sure the flat of top surface. CO<sub>2</sub> and H<sub>2</sub>O were introduced in the sample cell and the irradiation of 100 mW/cm<sup>2</sup> AM 1.5G was supplied. Timing begins when the irradiation was supplied, and the interval of sampling is 10 min.

## 7. DFT calculations

DFT calculations are performed with the plane wave based Vienna *Ab-initio* Simulation Package, VASP.<sup>5</sup> The calculations employ the generalized-gradient approximation (GGA) in the form of the Bayesian error estimation functional with van der Waals correlation (BEEF-vdW).<sup>6</sup> The interaction between the atomic cores and electrons is described by the projector augmented wave (PAW) method.<sup>7,8</sup> Valence wave functions are expanded in a plane wave basis with a cutoff energy of 400 eV. The top two layers of the five-layer slab are allowed to relax during local optimizations of the geometry until the force on each atom is less than 0.02 eV/Å. The Brillouin zone is sampled using a Monkhorst-Pack<sup>9</sup> mesh of 3×3×1  $k$  points for the (4×4) unit cells during geometry optimization. The binding free energy (BE) of an adsorbate is defined as  $BE = G_{ad/sub} - G_{ad} - G_{sub}$ , where  $G_{ad/sub}$  is the total free energy of the slab model with adsorbate, while  $G_{ad}$  and  $G_{sub}$  are the total free energies of the adsorbate in the gas phase (ground state) and of the clean substrate, respectively. Entropic contributions and zero point energies (ZPE) were taken into account, which converts DFT calculated energy into free energy. The entropy of adsorbate was calculated according to the Campbell's method with the following equation:<sup>10</sup>

$$S_{ads} = 0.7S_{gas} - 3.3R$$

where  $S_{ads}$  is the entropy of adsorbate;  $S_{gas}$  is the entropy of the corresponding gas-phase species, obtained from thermodynamic tables;<sup>11</sup> and R is the gas constant.

The implementation of the genetic algorithm (GA) is mainly based on the ones introduced by Chuang et al.,<sup>12</sup> Sierka<sup>13</sup> and Johnston.<sup>14</sup> The optimization is done with a six layer (2×2) (111) unit cell with top four layers allowed to be optimized during GA optimization. Test optimization with a larger (4×4) unit cell for PtCu<sub>3</sub> alloy converges to the same “global” minimum. In the initial generation, the population is selected to be twenty. The Pt and Cu atoms are randomly distributed in the top four layers, and are relaxed to the nearest local minimum. In order to reduce the computational cost, the cutoff energy of the plane wave basis is reduced to 280 eV during the structure optimization. After all individual optimization of current generation is finished, the 20<sup>th</sup> (same number as the population in the initial generation) most stable structures in all calculated generations are selected to be the survival of the fittest. They are used to generate the structures of the next generation by mating, which is achieved by combination of two randomly selected survival structures. We chose a combination method introduced by Chuang et al., which is achieved by cutting parent structures by an arbitrary plane perpendicular to the slab surface and recombining them. Each generated structure has 20% possibility to be mutated by atomic permutation, i.e. swapping the position of a randomly picked Pt-Cu pair. In order to increase the possibility to pass the structure information from the more stable structures to the new generated structures, the parent structure is chosen according to the roulette wheel selection, using an exponential fitness function with  $\alpha = 3$ .

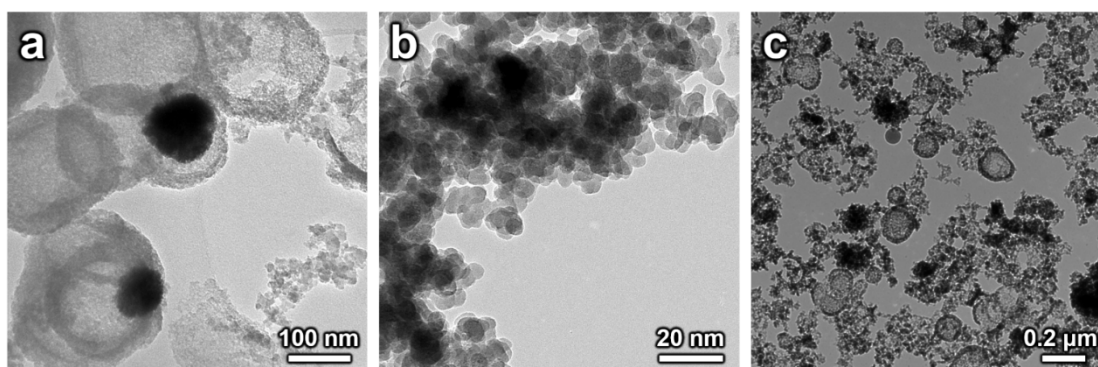


**Figure S1.** Failed intermediate morphologies during the formation of MTCP-MSs. (a) Aggregated CuPt alloy loaded on T-MSs using  $\text{H}_2\text{PtCl}_6$  and  $\text{Cu}(\text{NO}_3)_2$  as precursors in aqueous solution. (b) Modified Stöber method to synthesize  $\text{SiO}_2$  nanospheres loaded with  $\text{MnO}_x$  using  $\text{Mn}(\text{NO}_3)_2$  as the precursor.  $\text{Mn}^{2+}$  will react with hydroxide ions rapidly and then form  $\text{MnO}_x$  chunk, which will make it impossible to synthesize the  $\text{MnO}_x$ - $\text{SiO}_2$ . (c) Crashed  $\text{TiO}_2$  shells without the  $\text{SiO}_2$  outermost protective layers during the calcination.

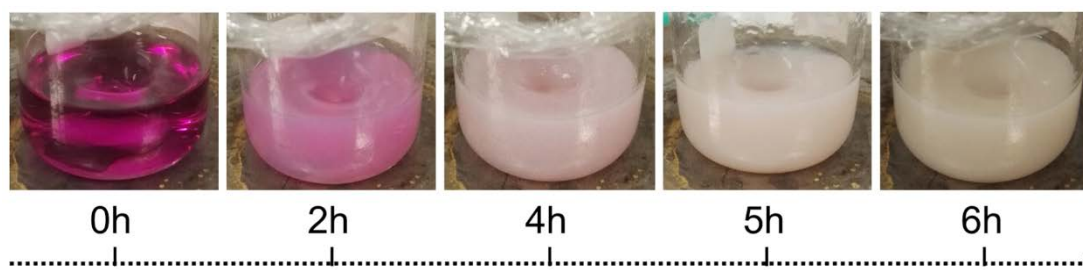


**Figure S2.** Modified Stöber method was used to synthesize  $\text{SiO}_2$  nanospheres with  $\text{MnO}_x$  uniformly loaded using  $\text{KMnO}_4$  as the precursor. The color of solutions turned from amaranth ( $\text{KMnO}_4$ ) to brown ( $\text{MnO}_x$ ) slowly, indicating the slow formation of  $\text{MnO}_x$  particles. Besides, the solution became more and more muddy, suggesting the formation of  $\text{SiO}_2$  nanospheres. Stöber method was generally used to synthesize  $\text{SiO}_2$  nanospheres in alkaline ethanol solutions by the slow hydrolysis of TEOS. Thus,  $\text{KMnO}_4$  with weekend oxidizability in alkaline surroundings would be slowly reduced by ethanol to  $\text{MnO}_x$ , resulting in small and uniformly distributed  $\text{MnO}_x$  particles.

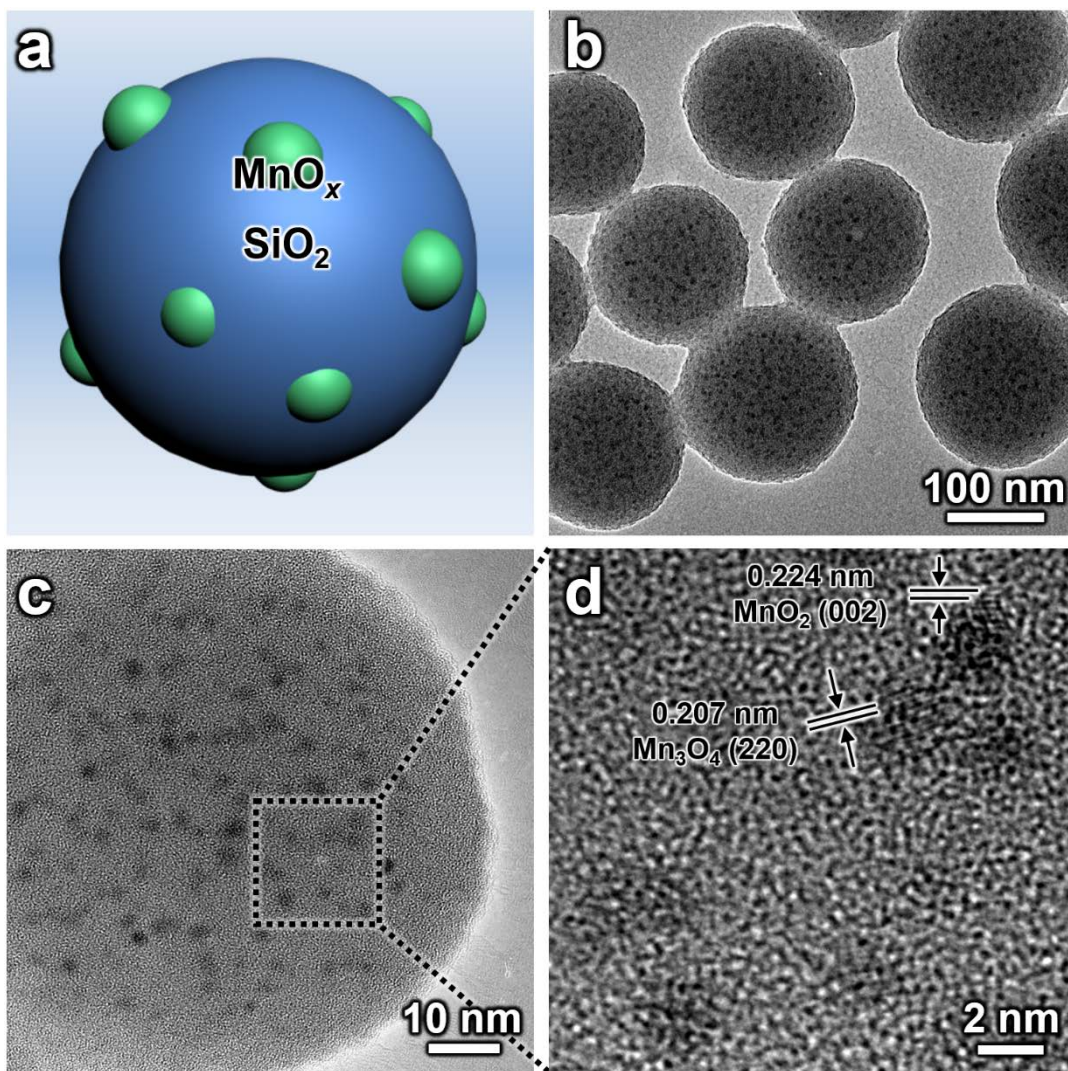


**Figure S3.** (a) Schematic model, (b-c) TEM images and (d) HRTEM image of SM-NSs.

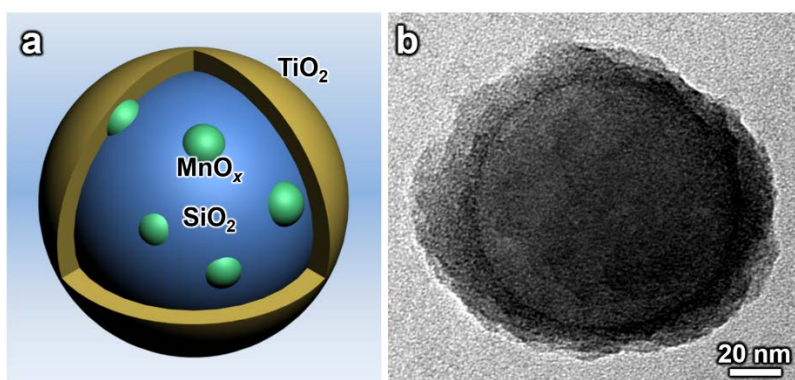


**Figure S4.** (a) Schematic model and (b) TEM image of SMT-NSs.

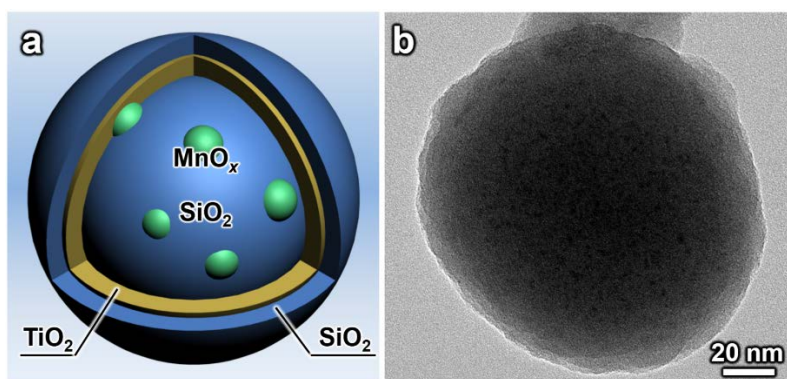


**Figure S5.** (a) Schematic model and (b) TEM image of SMTS-NSs.

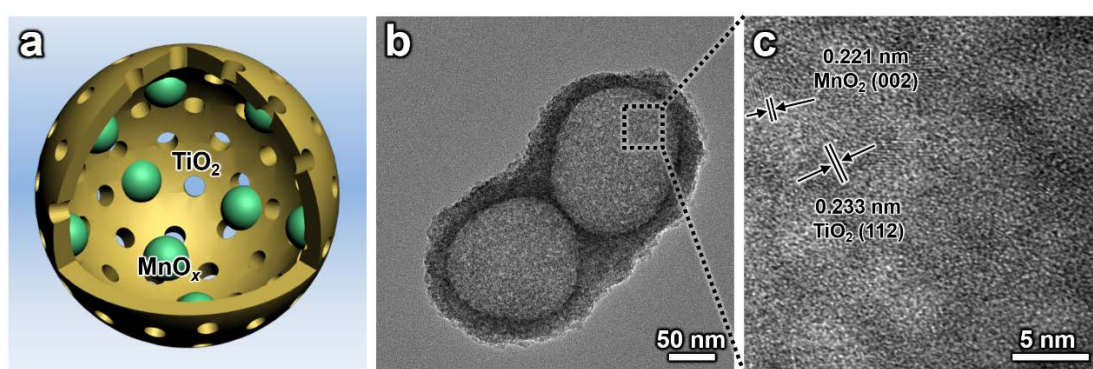


**Figure S6.** (a) Schematic model, (b) TEM image and (c) HRTEM image of MT-MSs.

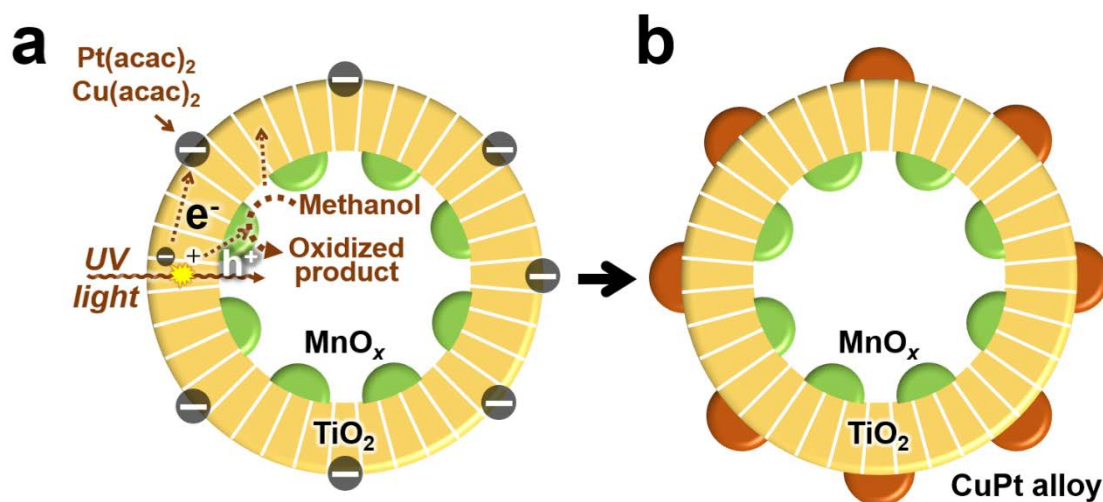


**Figure S7.** Selectively loaded CuPt alloys on the outer surface of MT-MSs.  $\text{Pt}(\text{acac})_2$  and  $\text{Cu}(\text{acac})_2$  were used as precursors during the deposition. After the generation of electrons and holes from  $\text{TiO}_2$  under irradiation, holes were trapped by  $\text{MnO}_x$  particles loaded on the inner surface and then consumed by sacrificial reagent (methanol), leaving electrons on the outer surface.  $\text{Pt}(\text{acac})_2$  and  $\text{Cu}(\text{acac})_2$  reacted with electrons to selectively load CuPt on the outer surface.

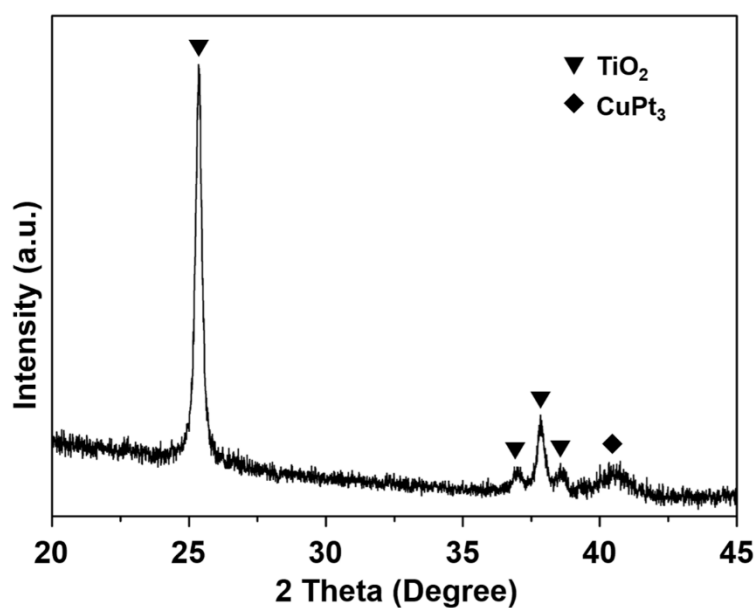


**Figure S8.** XRD patterns for  $\text{MnO}_x@ \text{TiO}_2@ \text{CuPt}_3$ . Peaks of  $\text{TiO}_2$ , and  $\text{CuPt}_3$  can be obviously observed. For  $\text{MnO}_x$  loaded inner the sphere and the loading is low and particle size is small, the signal of  $\text{MnO}_x$  is not obvious. Both the peaks of  $\text{TiO}_2$  can be attribute to anatase.

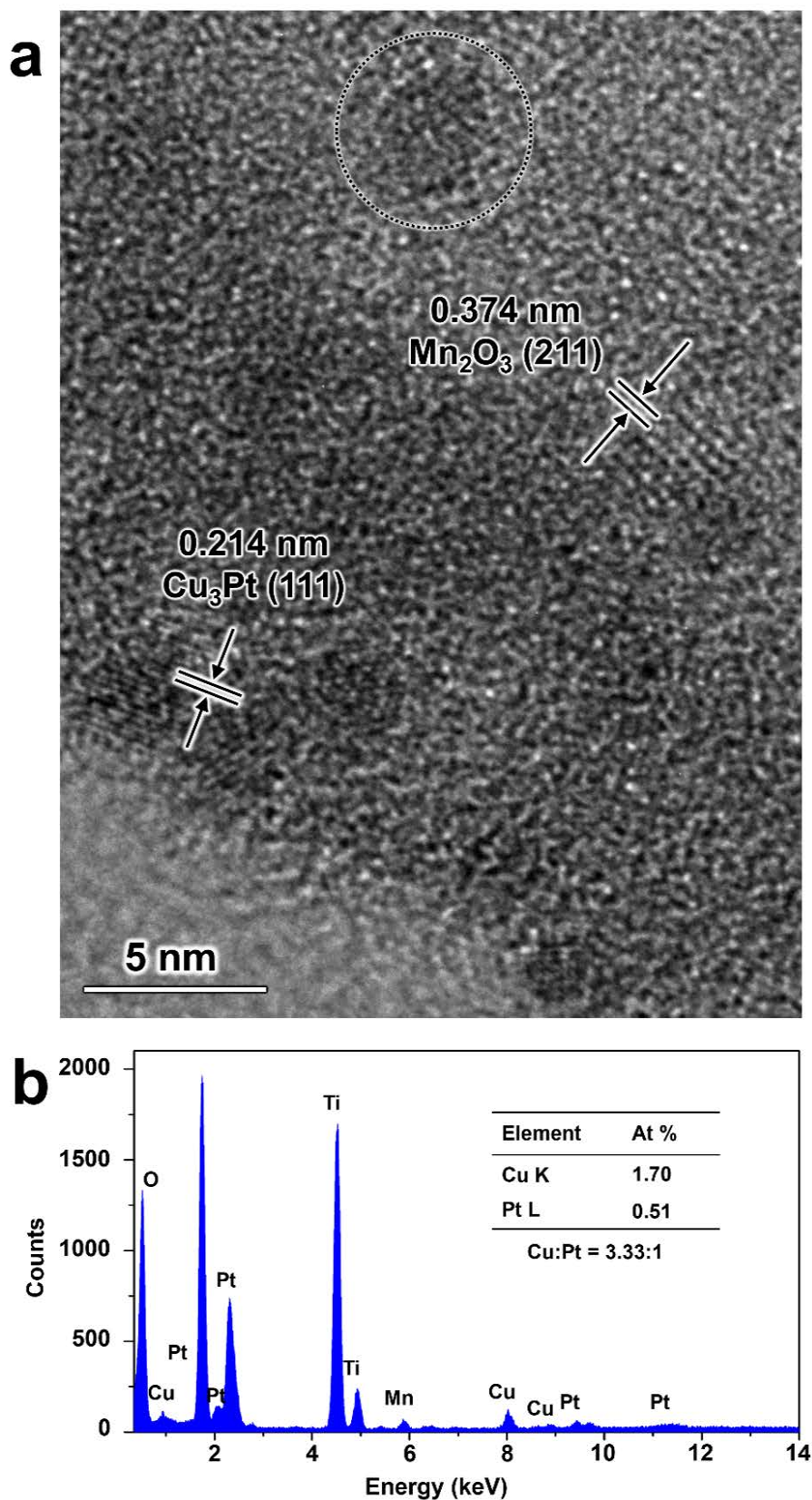


**Figure S9.** (a) HRTEM image and (b) EDS elemental analysis focused on single site (within the dotted circle of image a) of MTC<sub>3.17</sub>P-MSs confirms the relative position and components of every fraction.

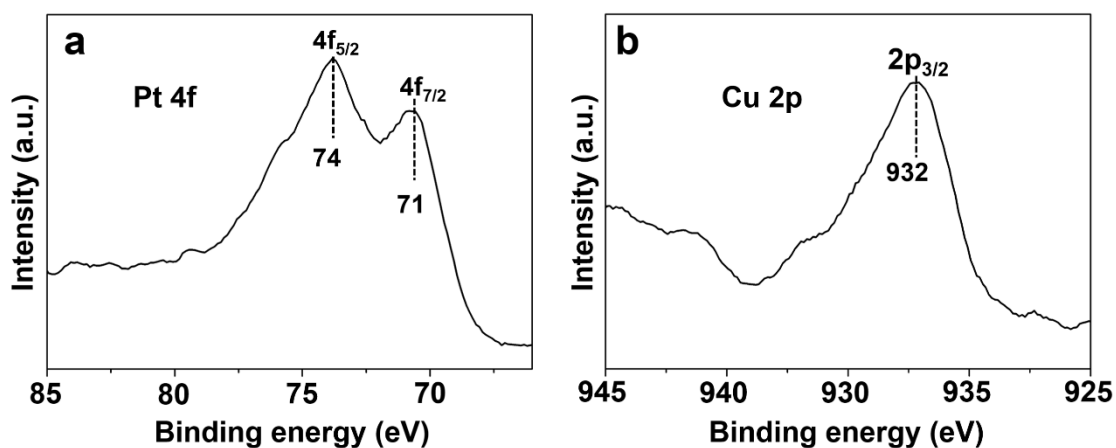


**Figure S10.** XPS patterns of MTC<sub>3.17</sub>P-MSs. (a) The single of Pt 4f. The banding energy of 74 eV, 71eV represents the Pt4f<sub>5/2</sub> and Pt4f<sub>7/2</sub> of CuPt alloy. (b) The single of Cu 2p. The banding energy of 932 eV represents the Cu2p<sub>3/2</sub> of CuPt alloy.

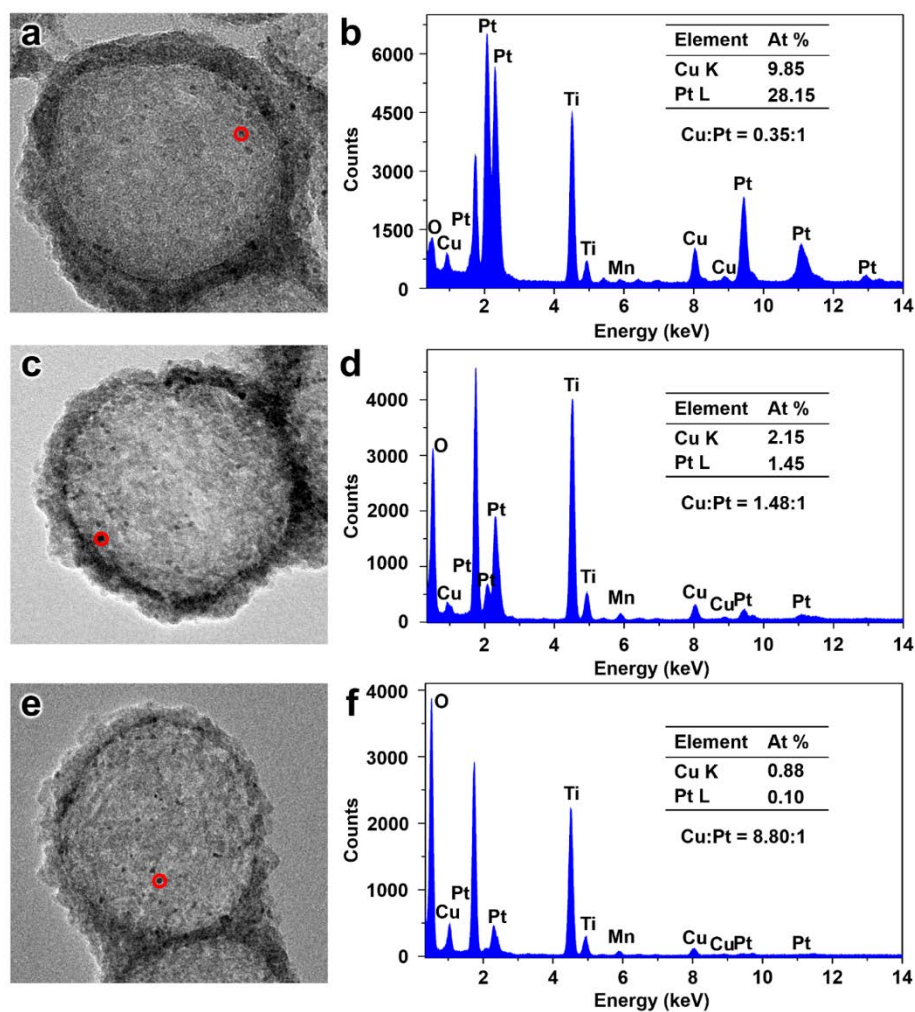


**Figure S11.** TEM images and EDS elemental analysis focused on small sites (within the red circles) of (a-b) MTC<sub>0.31</sub>P-MSs, (c-d) MTC<sub>1.13</sub>P-MSs and (e-f) MTC<sub>8.72</sub>P-MSs.

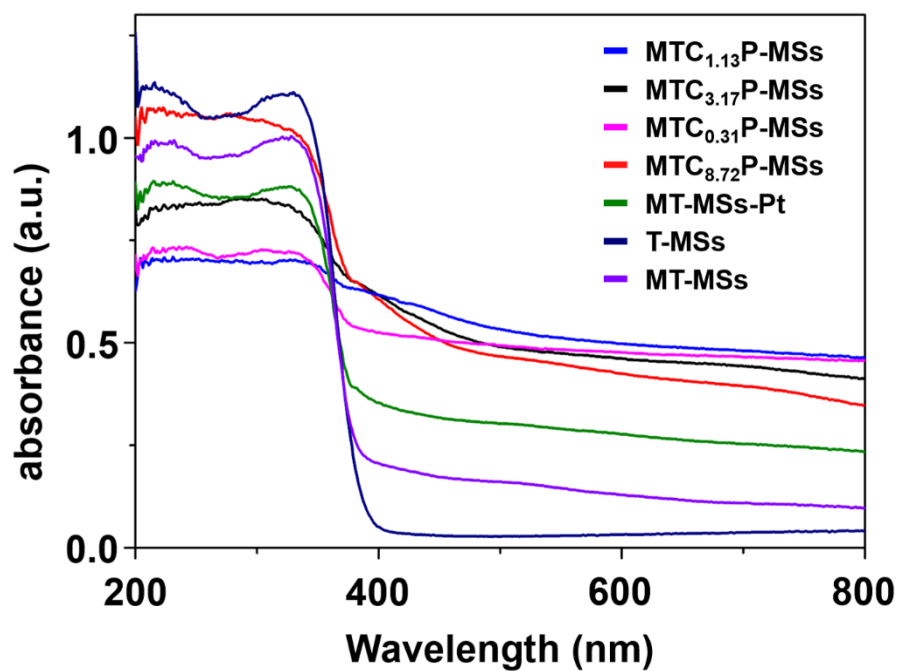


**Figure S12.** (a) UV-Vis of T-MSs, CuPt alloy loaded MT-MSs and Pt loaded MT-MSs.

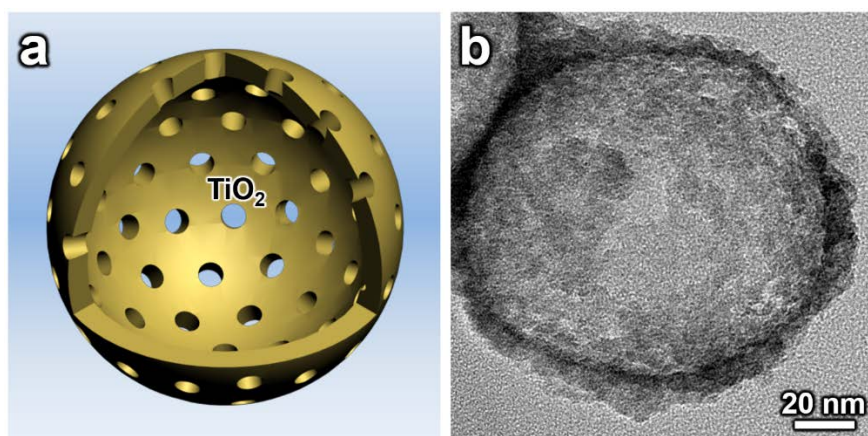


**Figure S13.** (a) Schematic model and (b) TEM image of T-MSs.

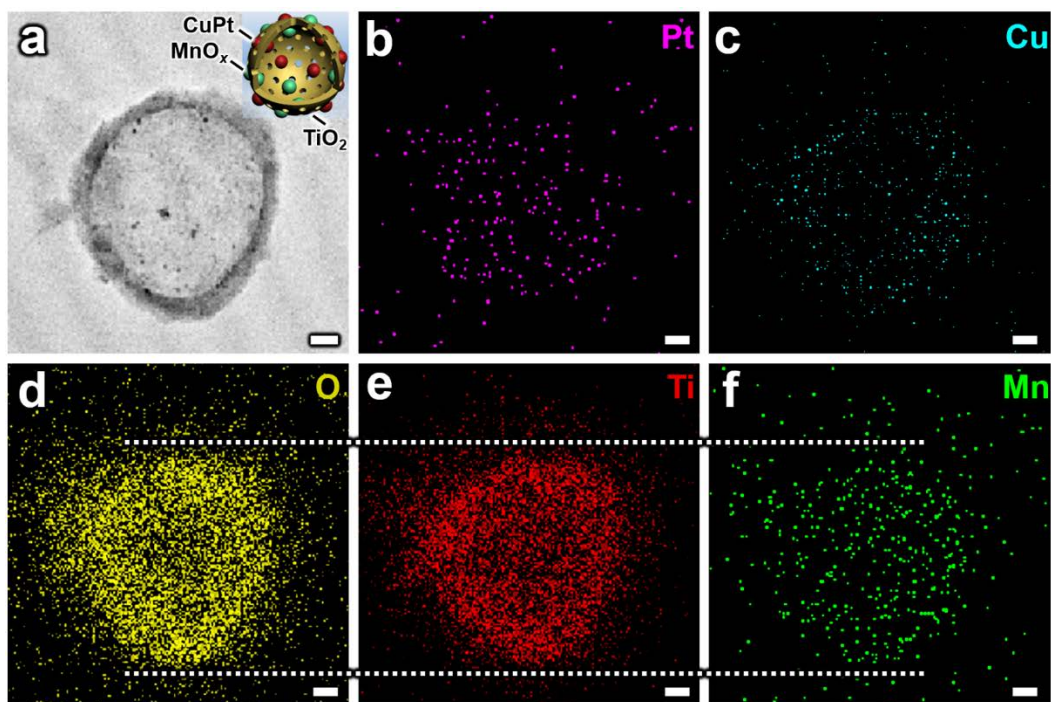


**Figure S14.** (a) TEM image and (b-f) EDS mapping of T/M/C<sub>3.21</sub>Pt-MSs. Corresponding elements are labelled on the upper right corner of every image. MnO<sub>x</sub> and CuPt particles are randomly distributed on both inner and outer surface of TiO<sub>2</sub> hollow spheres. Inset in image a is the schematic model of T/M/C<sub>3.21</sub>Pt-MSs.

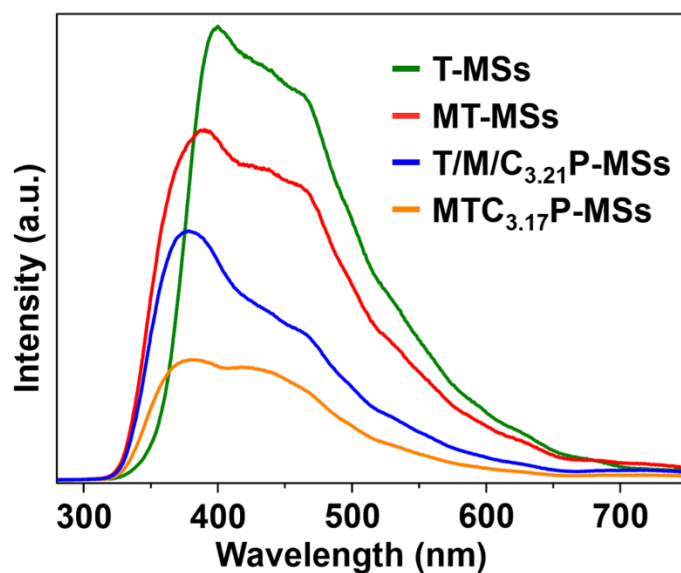


**Figure S15.** The steady state fluorescence (PL) spectra of catalysts with different structure.

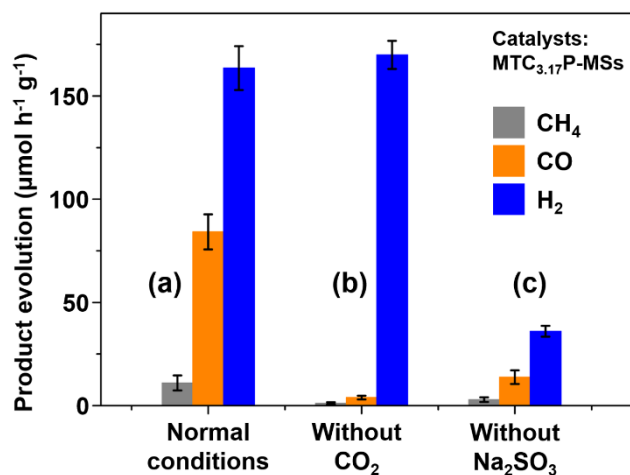


**Figure S16.** The Comparison of experiments under diverse reactive conditions over  $\text{MTC}_{3.17}\text{P-MSs}$ . a) normal conditions of photocatalytic reduction of  $\text{CO}_2$ . b) Photocatalytic reaction without the injection of  $\text{CO}_2$ . c) Photocatalytic reaction without  $\text{Na}_2\text{SO}_3$ .

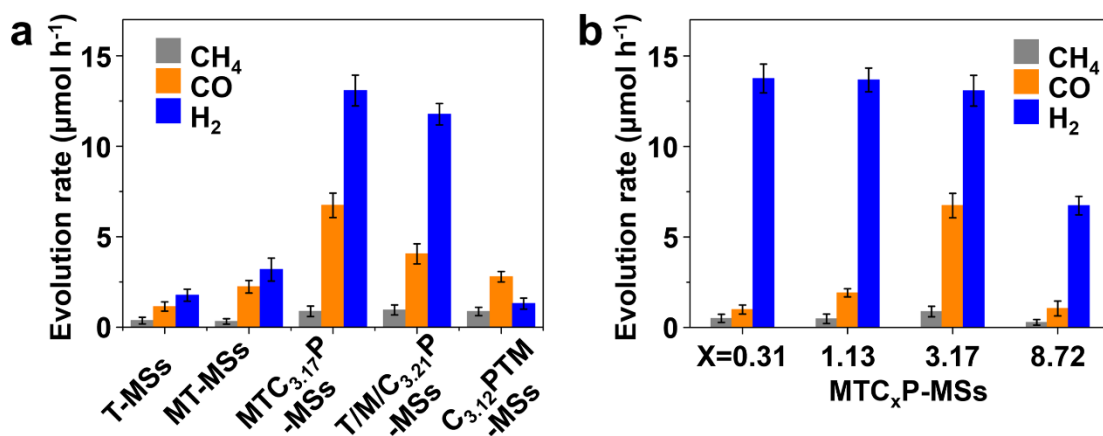


**Figure S17.** The rate of  $\text{CO}_2$  reduction products without normalization by catalyst weight over catalysts with different (a) morphology and (b) Cu contents.

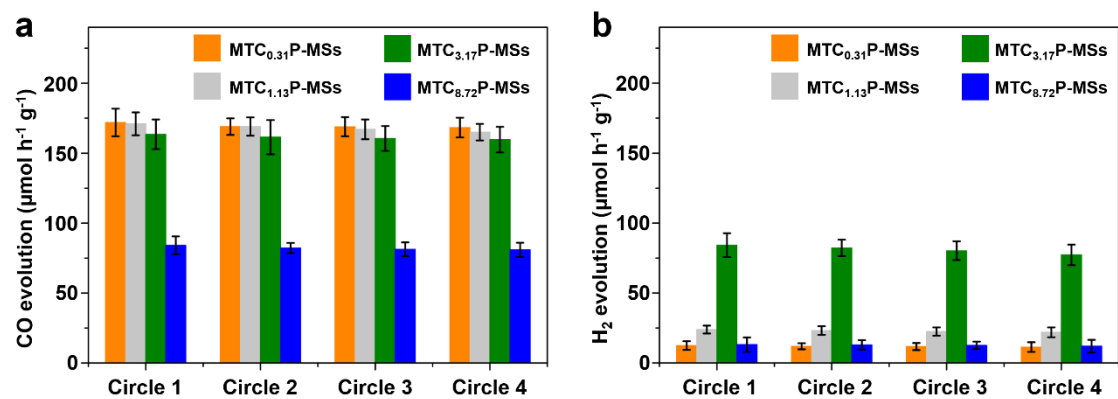


**Figure S18.** The investigation of stability during photocatalytic reaction. (a) CO generation during 4 circles over diverse catalysts. (b) H<sub>2</sub> generation during 4 circles over diverse catalysts.

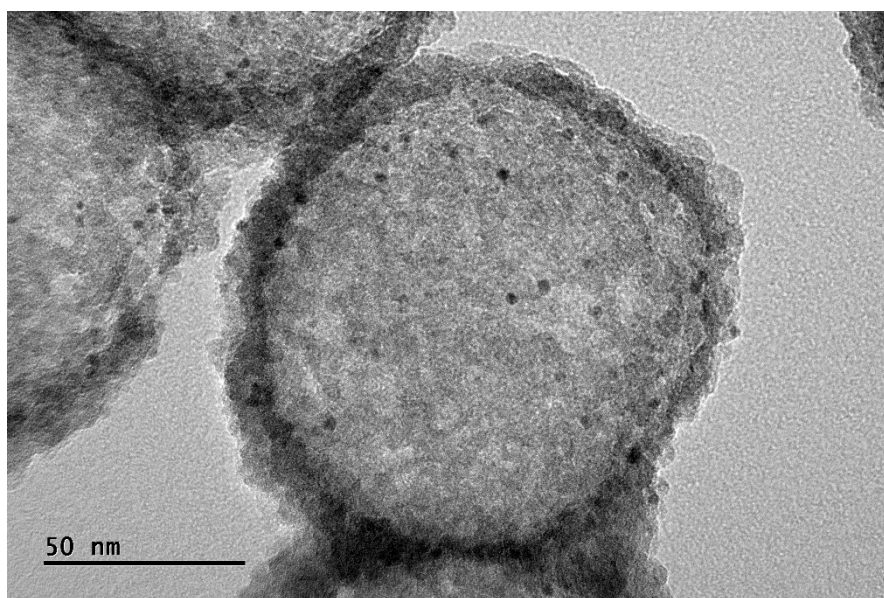


**Figure S19.** TEM image of MTC<sub>3.17</sub>P-MSs after the photocatalytic reaction.

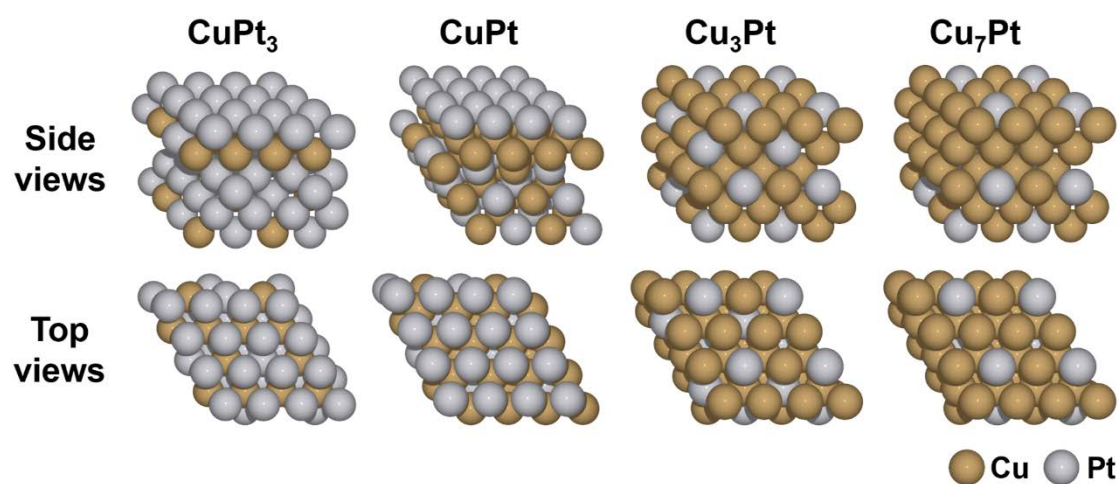


**Figure S20.** Models used in DFT calculation.

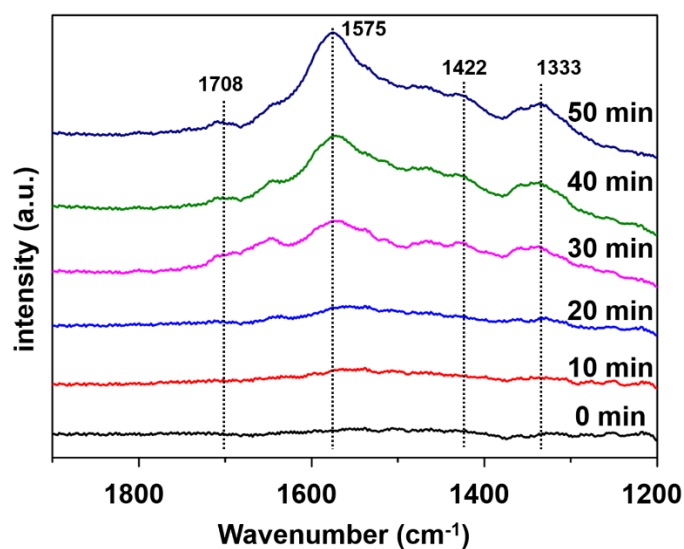


**Figure S21.** Patterns of the in-suit infrared spectrometer. Peaks at 1708, 1575, 1422 and 1333  $\text{cm}^{-1}$  of wavenumber can be assigned to the stretching vibration of C=O bond of carboxylic acid, the asymmetric stretching vibration of OCO of carboxyl, the symmetrical stretching vibration of  $\text{COO}^-$  of carboxyl and the stretching vibration of C-OH of carboxyl.<sup>2, 15, 16</sup>

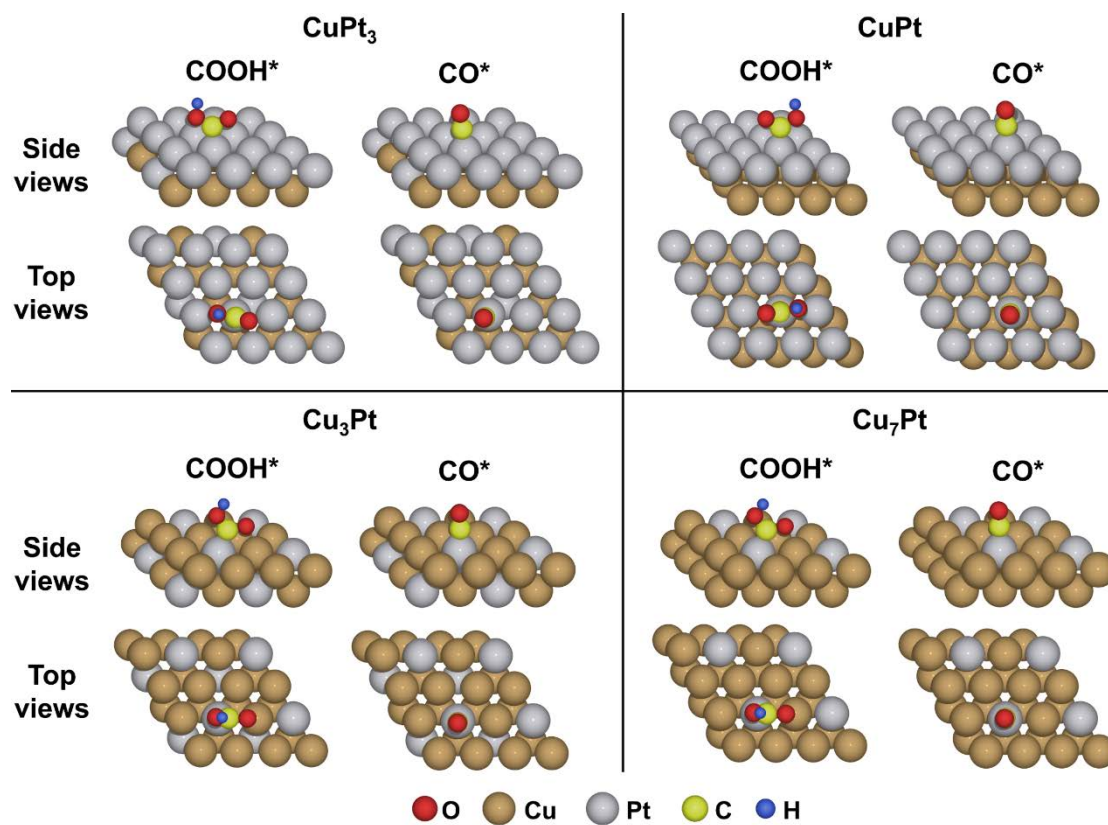


**Figure S22.** Models used in DFT calculation about every intermediate adopted on each catalyst.

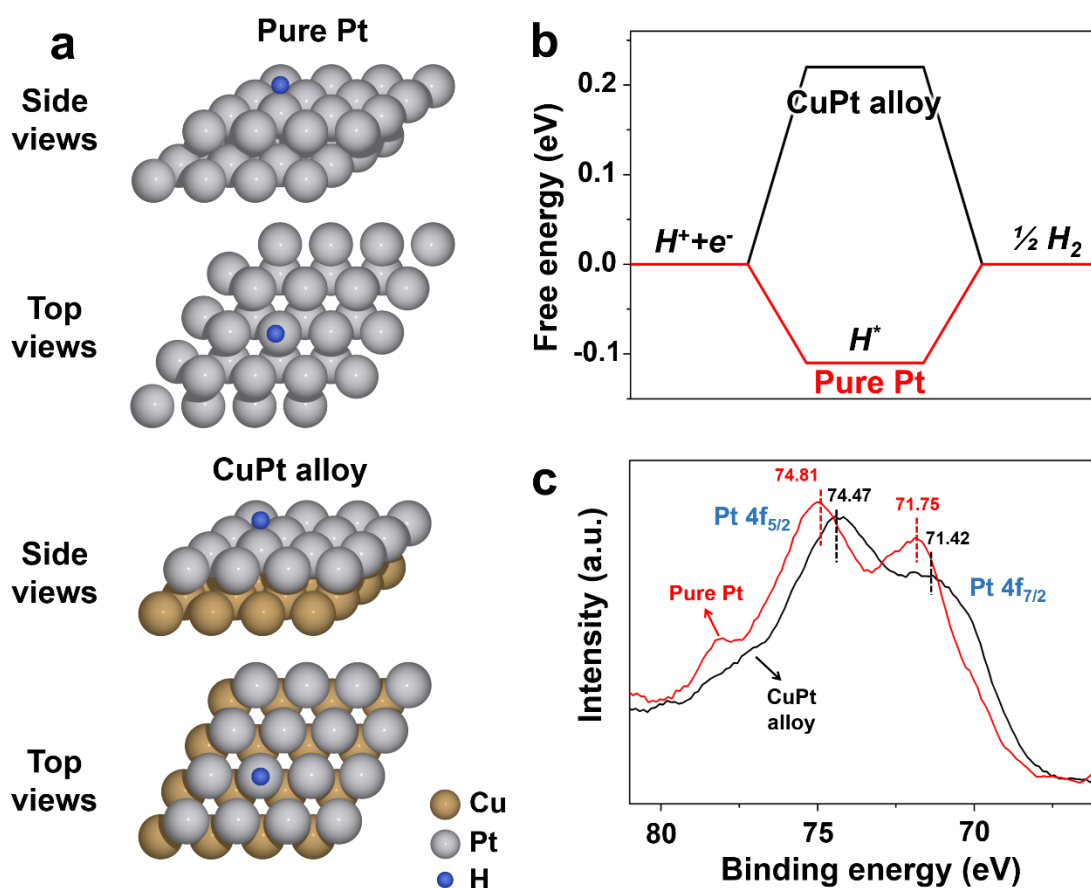


**Figure S23.** Illustration of the interaction between Cu and Pt in CuPt alloy and its influence of the competitive H<sub>2</sub> generation reaction. Typically, the energy barrier of H<sub>2</sub> generation over Pt or CuPt alloy follows two steps: (1) the adsorption of H<sup>+</sup> (H<sup>+</sup>+e<sup>-</sup>→2H\*); (2) the desorption of H<sub>2</sub> (H\*→1/2H<sub>2</sub>).<sup>17, 18</sup> (a) Models used in DFT calculation of H<sub>2</sub> generation over metals. (b) The change of free energy during the process of H<sub>2</sub> generation. Compared with pure Pt, the free energy of CuPt changed from -0.11 to 0.22 eV. Thus, for CuPt alloy, an energy barrier of 0.22 (0.22-0) eV should be overcome, which may be more difficult than overcoming the potential well of 0.11 (0-(-0.11)) eV when pure Pt is used. Thus, the addition of Cu to Pt to form an alloy could restrict the generation of H<sub>2</sub>.<sup>17-19</sup> (c) XPS spectra of Pt in pure Pt and CuPt alloy, which indicate the interaction between Cu and Pt. Compared with pure Pt, the addition of Cu lead to a c.a. 3.3 eV negative shift for the peaks of Pt, indicating the enriched electron density around Pt.<sup>20</sup> Thus, in CuPt alloy, the interaction of Cu and Pt may lead to the transfer of electrons from Cu to Pt.<sup>21</sup> Additionally, the enriched electron density around Pt may lead to the rise of free energy, which supports the calculation result shown in [Figure S23b](#).

**Table S1.** The evolution rate of CO<sub>2</sub> reduction products without normalization by catalyst weight over all catalysts.

Catalysts	Evolution rate of every product ( $\mu\text{mol h}^{-1}$ )		
	CH <sub>4</sub>	CO	H <sub>2</sub>
T-MSs	$0.37 \pm 0.18$	$1.15 \pm 0.26$	$1.77 \pm 0.33$
MT-MSs	$0.32 \pm 0.15$	$2.24 \pm 0.34$	$3.19 \pm 0.63$
MTC <sub>3.17</sub> P-MSs	$0.88 \pm 0.29$	$6.73 \pm 0.68$	$13.08 \pm 0.85$
T/M/C <sub>3.21</sub> P-MSs	$0.96 \pm 0.27$	$4.06 \pm 0.55$	$11.77 \pm 0.59$
C <sub>3.12</sub> PTM-MSs	$0.87 \pm 0.23$	$2.79 \pm 0.29$	$1.31 \pm 0.30$
MTC <sub>0.31</sub> P-MSs	$0.50 \pm 0.22$	$0.99 \pm 0.25$	$13.75 \pm 0.79$
MTC <sub>1.13</sub> P-MSs	$0.48 \pm 0.26$	$1.91 \pm 0.22$	$13.68 \pm 0.66$
MTC <sub>3.17</sub> P-MSs	$0.88 \pm 0.29$	$6.73 \pm 0.68$	$13.08 \pm 0.85$
MTC <sub>8.72</sub> P-MSs	$0.29 \pm 0.15$	$1.05 \pm 0.40$	$6.73 \pm 0.51$

**Table S2.** The comparison of Cu contents between model catalysts and corresponding real catalysts.

Experiment		Model	
Real catalysts	Cu content / %	Model catalysts	Cu content / %
MTC <sub>0.31</sub> P-MSs	23.7	CuPt <sub>3</sub>	25.0
MTC <sub>1.13</sub> P-MSs	53.1	CuPt	50.0
MTC <sub>3.17</sub> P-MSs	76.0	Cu <sub>3</sub> Pt	75.0
MTC <sub>8.72</sub> P-MSs	89.7	Cu <sub>7</sub> Pt	87.5

## References

1. R. Purbia and S. Paria, *Nanoscale*, 2015, **7**, 19789-19873.
2. X. Jiao, X. Li, X. Jin, Y. Sun, J. Xu, L. Liang, H. Ju, J. Zhu, Y. Pan, W. Yan, Y. Lin and Y. Xie, *J. Am. Chem. Soc.*, 2017, **139**, 18044-18051.
3. L. Liu, C. Zhao and Y. Li, *J. Phys. Chem. C*, 2012, **116**, 7904-7912.
4. L. Liu, C. Zhao, D. Pitts, H. Zhao and Y. Li, *Catal. Sci. Technol.*, 2014, **4**, 1539-1546.
5. G. Kresse and J. Furthmüller, *Phys. Rev. B*, 1996, **54**, 11169.
6. J. Wellendorff, K. T. Lundgaard, A. Møgelhøj, V. Petzold, D. D. Landis, J. K. Nørskov, T. Bligaard and K. W. Jacobsen, *Phys. Rev. B*, 2012, **85**, 235149.
7. P. E. Blöchl, *Phys. Rev. B*, 1994, **50**, 17953.
8. G. Kresse and D. Joubert, *Phys. Rev. B*, 1999, **59**, 1758.
9. H. J. Monkhorst and J. D. Pack, *Phys. Rev. B*, 1976, **13**, 5188.
10. C. T. Campbell, L. Árnadóttir and J. R. Sellers, *Z. Phys. Chem.*, 2013, **227**, 1435-1454.
11. W. M. Haynes, in *CRC Handbook of Chemistry and Physics*, 95th ed. W. M. Haynes, D. R. Lide; and T. J. Bruno, CRC Press, Boca Raton, 2014, pp. 5-4 - 5-42.
12. F. Chuang, C. V. Ciobanu, V. Shenoy, C.-Z. Wang and K.-M. Ho, *Surf. Sci.*, 2004, **573**, L375-L381.
13. M. Sierka, *Prog. Surf. Sci.*, 2010, **85**, 398-434.
14. R. L. Johnston, *Dalton T.*, 2003, 4193-4207.
15. S. Kattel, W. Yu, X. Yang, B. Yan, Y. Huang, W. Wan, P. Liu and J. G. Chen, *Angew. Chem. Int. Ed.*, 2016, **55**, 7968-7973.
16. S. Weng, *Analysis with Fourier Transform Infrared Spectroscopy*, Chemical Industry Press, Beijing, 2010.
17. Z. W. Seh, J. Kibsgaard, C. F. Dickens, I. Chorkendorff, J. K. Nørskov and T. F. Jaramillo, *Science*, 2017, **355**.
18. Z. Chen, Y. Song, J. Cai, X. Zheng, D. Han, Y. Wu, Y. Zang, S. Niu, Y. Liu, J. Zhu, X. Liu and G. Wang, *Angew. Chem. Int. Ed.*, 2018, **57**, 5076-5080.
19. A. J. Medford, A. C. Lausche, F. Abild-Pedersen, B. Temel, N. C. Schjødt, J. K. Nørskov and F. Studt, *Top. Catal.*, 2013, **57**, 135-142.
20. S. Zhang, P. Kang and T. J. Meyer, *J. Am. Chem. Soc.*, 2014, **136**, 1734-1737.
21. M. D. Marcinkowski, M. T. Darby, J. Liu, J. M. Wimple, F. R. Lucci, S. Lee, A. Michaelides, M. Flytzani-Stephanopoulos, M. Stamatakis and E. C. H. Sykes, *Nature Chem.*, 2018, **10**, 325-332.